Vol. 54: 69–84, 2012
doi: 10.3354/cr01101

CLIMATE RESEARCH
Clim Res

Published online August 22

Response of clouds and surface energy fluxes to changes in sea-ice cover over the Laptev Sea (Arctic Ocean)

Neil P. Barton[1,*], Dana E. Veron[2]

[1]Program for Climate Model Diagnosis and Intercomparison, Lawrence Livermore National Laboratory, Livermore, California 94551, USA

[2]College of Earth, Ocean, and Environment, University of Delaware, Newark, Delaware 19716, USA

ABSTRACT: The response of Arctic clouds to changes in sea ice extent is examined using the Polar version of the Weather Research and Forecasting (WRF) regional model over the Laptev Sea. Polar WRF output provides detailed information on cloud properties, such as liquid water path, ice water content, cloud height, and cloud radiative forcing during periods of low and high sea ice extent. The Polar WRF is run for 8 Septembers and Octobers selected for anomalously low and high sea ice cover, and analyzes differences in cloud properties, cloud radiative forcing (CRF), temperature, and the surface radiative and heat budgets. Clouds were more frequent and had larger liquid water paths during low than during high sea ice cover years. Increased surface longwave CRF during the low sea ice years only occurred in September. In September, the averaged cloud liquid water path during high sea ice years resulted in a cloud emitting close to its maximum longwave radiation, and increases in cloud liquid water path during the low sea ice years did not increase the surface longwave cloud radiative effect. In October, the averaged cloud liquid water path during high sea ice years did not result in a cloud emitting its maximum longwave radiation, and cloud liquid water path increases that occurred in the low sea ice years affected the surface cloud radiative effect. Clouds warmed the surface during periods of low sea ice cover in October.

KEY WORDS: Sea ice · Clouds · Arctic · Polar Weather Research and Forecasting · Laptev Sea

1. INTRODUCTION

The interplay of Arctic clouds, sea ice, and near-surface temperature is important when examining Arctic climate change. Arctic cloud coverage is predicted to increase and alter the surface radiative budget in an enhanced CO_2 environment (Miller & Russell 2002, Vavrus 2004, Miller et al. 2007). Changes in sea ice extent play a significant role in Arctic climate due to the associated variations in albedo, temperature, and moisture (Manabe & Bryan 1985, Paluch et al. 1997, Serreze & Francis 2006, Deser et al. 2010). Arctic clouds alter with changes in sea ice cover. This has been shown with surface observations (Eastman & Warren 2010), remotely sensed data (Schweiger et al. 2008a, Kay & Gettelman 2009, Palm et al. 2010, Kay et al. 2011) and observational-constrained models (Schweiger et al. 2008, Cuzzone & Vavrus 2011, Kay et al. 2011). Covariance occurred between cloud cover and sea ice cover in these studies, but the cloud response differed as a function of atmospheric height. For example, some studies found that Arctic open water areas had a smaller cloud amount at the lowest atmospheric levels, compared to sea ice periods (Schweiger et al. 2008b, Palm et al. 2010, Cuzzone & Vavrus 2011, Kay et al. 2011). Kay & Gettelman (2009) found that Arctic open water areas have larger cloud amounts close to the surface than sea ice covered areas; this is an apparent contradiction to the other studies, but there are many differences among these

*Email: barton30@llnl.gov

studies, such that a direct comparison is not possible. In all of the above-mentioned studies, clouds at some height above the surface increased during open water periods, compared to sea ice covered periods.

Cloud cover changes do not necessarily represent a change in the surface radiative cloud effect. Changes in cloud properties (e.g. liquid water path [LWP], ice water path [IWP], cloud base height, and cloud optical depth) are important for determining the cloud effect on the surface radiative budget (Shupe & Intrieri 2004, Chen et al. 2006). Palm et al. (2010) determined that cloud optical depth increased at altitudes >500 m during periods of open water, compared to periods of sea ice. Kay et al. (2011) reported increases in LWP during the September 2007 sea ice condition compared to the climatologically averaged sea ice conditions. This increase in LWP resulted in clouds slightly warming the surface in the longwave and slightly cooling the surface in the total radiative budget. Schweiger et al. (2008a) reported differences in the surface net energy budget between open water and sea ice covered years averaged for the fall season (September, October, and November), and only found differences of ~1 W m^{-2}. One-dimensional modeling studies indicated that variations in cloud cover are important for determining changes in Arctic surface radiative, snow, and sea ice properties (Shine & Crane 1984, Curry & Ebert 1992, Curry et al. 1993, Beesley 2000). However, further study is needed into the detailed changes between the surface radiative budget, clouds, cloud radiative effect, and sea ice extent.

We examine changes in cloud properties, surface radiative properties, and surface heat fluxes in 2 autumn months during years with low and high sea ice cover using the Polar version of the Weather Research and Forecasting (WRF) model. Recent developments (Morrison et al. 2005, Hines & Bromwich 2008, Bromwich et al. 2009) in the Polar WRF have improved the ability to investigate Arctic climate variability at high spatial and temporal resolutions. In the present study, the radiative, cloud, and heat flux responses to changes in sea ice cover are examined in September and October. At this time, sea ice is at its lowest extent and beginning to reform. Unlike previous studies, we focused on the Laptev Sea, where sea ice cover varies little during the period of study. This is unique relative to the above-mentioned studies in that we analyzed the response of clouds to changes in sea ice by removing long term sea ice and climate trends. However, the dynamics and thermodynamics in the Laptev Sea may not be representative of all Arctic regions. Also unique to the present study, we employ data with a higher temporal frequency in addition to monthly results.

2. MODEL DESCRIPTION

Parameterizations provided by the Byrd Polar Research Group at Ohio State University were employed in a configuration commonly known as Polar WRF, which has been tested in the Arctic in regions such as the Greenland ice sheet (Hines & Bromwich 2008), the Arctic Ocean (Bromwich et al. 2009), the Arctic landmass (Hines et al. 2011), and throughout the Arctic domain (Wilson et al. 2011). Bromwich et al. (2009) employed Polar WRF over the Surface Heat Budget of the Arctic Ocean (SHEBA) site for January, June, and August of 1998. The authors noted that differences between Polar WRF output and surface observations were associated with synoptic meteorological events and the representation of clouds. During the winter months, Polar WRF underpredicted cloud liquid water paths, which led to lower surface temperatures in the model compared to the SHEBA observations. The comparison of Polar WRF to observations was most favorable when the model correctly simulated cloud amount. For example, Bromwich et al. (2009) noted that at times when the surface pressure was overpredicted in Polar WRF by a few hPa, an underproduction of clouds also occurred.

From here on, the terms WRF or Polar WRF refer to the model configurations described below. The suite of parameterizations employed is similar to that used by Bromwich et al. (2009). The Atmospheric Research core of WRF (ARW) version 3.1.1 is utilized with the Morrison et al. (2005) 2-moment microphysics scheme. The Community Atmospheric Model version 3 (CAM3) (Collins et al. 2006) longwave and shortwave radiative schemes are used. The radiation scheme allows for multiple reflections, which is important over sea ice (DeWeaver et al. 2008). In addition, we employed the Grell & Devenyi (2002) cumulus scheme and the Mellor-Yamada-Janjic boundary layer scheme along with the Eta similarity surface layer scheme (Janjic 2002). Over water surfaces in Polar WRF, the surface layer scheme predicts the surface fluxes, which are computed following Janjic (1994). The NOAH land surface model (LSM) (Chen & Dudhia 2001), which is employed over solid surfaces (land and sea ice), is used with the polar modifications described by Hines & Bromwich (2008) and Bromwich et al. (2009). An important update to the polar LSM relative to the typical LSM is in the upward longwave flux calculation, which is now a function of skin tem-

perature instead of the boundary layer atmospheric temperature, because the Arctic skin temperature is generally much lower than that of the lowest boundary layer in the Arctic winter months.

The WRF cloud fraction (CF) is examined in the results and depends on the radiation scheme used. For the CAM3 radiation schemes, CF ranges from 0 to 1, is loosely based on Hong et al. (1998) and is described in Eq. (1), where RH is the relative humidity, and γ is a function of the cloud mixing ratio. The $(1 - e^{\gamma})$ term reduces cloud fractions when low cloud mixing ratios occur.

$$CF = RH^{0.25} (1 - e^{\gamma}) \quad (1)$$

The major boundary and initial conditions for Polar WRF are taken from ERA-40 reanalysis data, the National Centers for Environmental Prediction 2 (NCEP2) reanalysis (Kanamitsu et al. 2002) data, and Special Sensor Microwave Imager (SSM/I) retrievals. Polar WRF reads and uses ERA-40 atmospheric boundary conditions every 6 h. The atmospheric input variables include geopotential height, temperature, zonal winds, meridional winds, and relative humidity at 24 unequally spaced atmospheric levels from 1000 hPa to 1 hPa. Skin temperatures from NCEP2 reanalysis are assigned to the sea surface temperatures.

A major improvement in WRF version 3.1 is the input of fractional sea ice. For the runs described in the present study, daily fractional sea ice data from SSM/I, archived at the National Snow and Ice Data Center (NSIDC), are used as input. The sea ice data are archived on a polar stereographic grid with a resolution of 25 × 25 km. For this reason, Polar WRF is set up on a 25 × 25 km Lambert conformal grid. Polar WRF inputs sea ice cover every 6 h, but these data only change in the SSM/I dataset once a day. Sea ice cover is solely determined by the input data and cannot change based on atmospheric conditions. The sea ice albedo is set to 0.8, which is a reasonable value for reforming sea ice occurring in the fall months (Perovich et al. 2002). The model is initialized every day and runs for 48 h. The first 24 h of data are discarded as spin up, consistent with Bromwich et al. (2009). WRF outputs data every 2 h.

3. METHODS

3.1. Selection of high and low sea ice ensemble members

Data used for boundary and initial conditions overlap in availability from 1988 to October 2001. Before 1988, updates in the SSM/I sea ice cover occur every 2 d, and the ERA-40 reanalysis ends in August 2002. We isolate the sea ice–cloud relationship as much as possible from other large-scale climatic trends and focus on a location that does not have large linear trends in sea ice cover. Within this period of 1988 to 2001, locations in the northern Atlantic Ocean and north of Russia demonstrate strong negative linear trends in sea ice cover, i.e. sea ice decreases throughout the 13 yr period (Fig. 1). The sea ice cover in the Laptev Sea does not demonstrate any significant linear trend, so the WRF grid is centered at 77.5° N and 124.3° E (the Laptev Sea).

Sea ice cover from the SSM/I over the Laptev Sea is averaged for each September and October from 1988 to 2001, and the 4 years with the lowest and highest sea ice cover are selected (Table 1). There is an even temporal distribution of low and high sea ice autumns throughout the data set (Table 1). The differences in sea ice cover derived from the SSM/I between the averaged low and high sea ice Septembers and Octobers are shown in Fig. 2. The maximum differences in sea ice cover are >50.

To examine variability in cloud properties associated with sea ice cover, Polar WRF is run during September and October over the Laptev Sea for the years shown in Table 1, and the results are averaged for the ensemble low and high sea ice years. This experimental design follows the mesoscale modeling studies of Previdi & Veron (2005, 2007) and Strey et al. (2010).

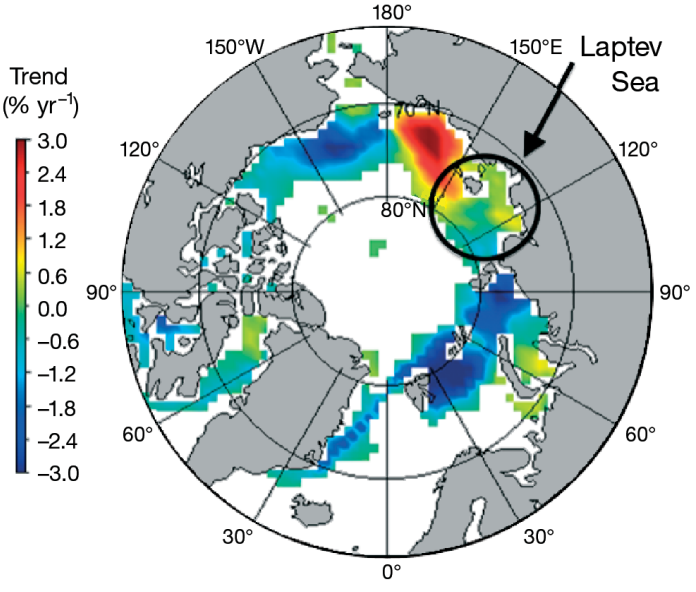

Fig. 1. Averaged September and October sea ice cover linear trend (% yr^{-1}) from 1988 to 2001 calculated using data from the Special Sensor Microwave Imager (SSM/I)

Table 1. High and low sea ice years used for the Polar Weather Research and Forecasting (WRF) runs, and Special Sensor Microwave Imager (SSM/I) sea ice and Advance very high resolution radiometer Polar Pathfinder eXtended (APP-X) cloud cover data (Wang & Key 2003) bounded by the region 72° N to 80° N and 110° E to 150° E. The differences in sea ice cover are significant

	Year	Ice cover (%)	Cloud cover (%)
Low extent	1990	60	68
	1994	69	70
	1995	44	81
	2000	60	80
High extent	1989	78	60
	1992	86	61
	1996	97	61
	1998	80	68

Because many of the results presented in this article are averages between the high and low sea ice years/ensembles across the Laptev Sea domain, it is important to test that the variability within the composites is not larger than the differences between the high and low sea ice years. To do this, 2 methods are used. The first method is the 2-tailed Student's *t*-test, where the null hypothesis is that the means and variances of the 2 distributions are equal. At locations with $p < 0.05$, the null hypothesis can be rejected with a confidence level of 95%.

The second method follows Klingaman et al. (2008), in which the standard deviation of the differences (Eq. 2) is normalized by the mean of the differences (Eq. 3).

$$S(X) = \left(\frac{1}{n} \sum_{i=1}^{n} \left\{ [L_i(X) - H_i(X)] - \left[\overline{L(X)} - \overline{H(X)} \right] \right\}^2 \right)^{1/2} \quad (2)$$

$$N(X) = \frac{S(X)}{\left| \overline{L(X)} - \overline{H(X)} \right|} \quad (3)$$

In Eq. (2), L_i represents a low sea ice year, H_i represents a high sea ice year, the over-bars represent the mean of the composites, X is the variable examined, and i represents all combinations of $L_i - H_i$. In Eq. (3), $N(X)$ is the ratio of the variance of the differences over the absolute value of the mean of the difference. Values <1 indicate that the variability in the differences is less than the mean of the differences. At the locations that were statistically significant based on Student's *t*-test, the variance of the difference of means was less than the difference of means. For simplicity, only Student's *t*-test results are shown.

3.2. Variable definitions

Surface radiative (Eq. 4) and surface energy (Eq. 5) budgets are defined as follows:

$$Q_{rad} = L\downarrow - L\uparrow + S\downarrow - S\uparrow \quad (4)$$

$$Q = L\downarrow - L\uparrow + S\downarrow - S\uparrow - LH - SH \quad (5)$$

Q_{rad} is the net surface radiative budget, Q is the net surface heat budget, $L\downarrow$ is the downwelling longwave radiation, $L\uparrow$ is the upwelling longwave radiation, $S\downarrow$ is the downwelling shortwave radiation, $S\uparrow$ is the upwelling shortwave radiation, LH is the latent heat flux, and SH is the sensible heat flux. All values are derived at the surface, and positive values of Q_{rad} and Q represent fluxes toward the surface.

To quantitatively examine the changes in $L\downarrow$ and $S\downarrow$ that are caused by clouds, the cloud radiative forcing (CRF) (Ramanathan et al. 1989) is calculated. CRF_{total} is the sum of the shortwave (CRF_{SW}) and longwave (CRF_{LW}) components:

$$CRF_{total} = CRF_{LW} + CRF_{SW} \quad (6)$$

where CRF_{LW} and CRF_{SW} are defined as follows:

$$CRF_{LW} = L\downarrow(C) - L\downarrow(0) \quad (7)$$

$$CRF_{SW} = S\downarrow(C) - S\downarrow(0) \quad (8)$$

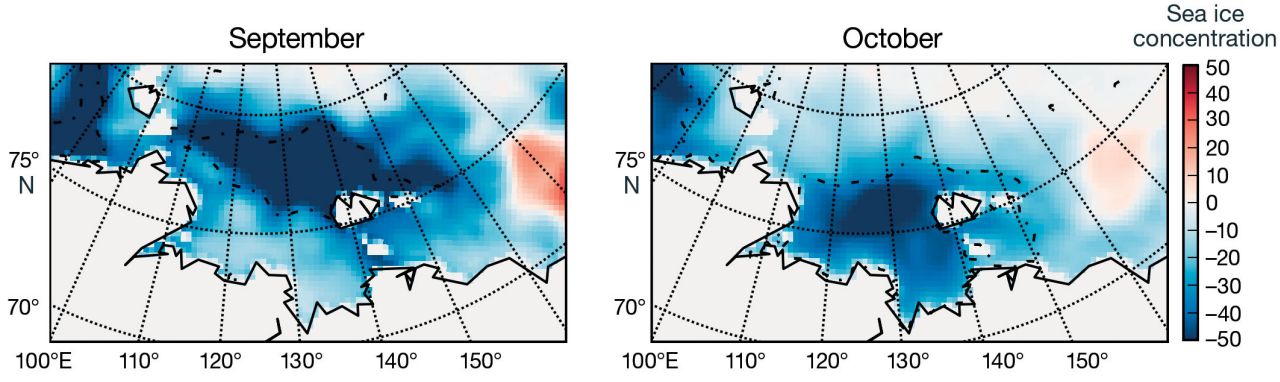

Fig. 2. Averaged SSM/I sea ice concentration during low sea ice cover years minus high sea ice cover years in September and October. The dot-dash line contours regions with $p < 0.05$. The low and high years are shown in Table 1

where $L\downarrow$(C) and $S\downarrow$(C) are the longwave and shortwave all-sky downwelling fluxes, and $L\downarrow$(0) and $S\downarrow$(0) are the clear-sky longwave and shortwave fluxes. Positive values of CRF represent clouds having a warming effect, and negative values represent a cooling effect.

CRF is defined at the surface, and WRF outputs all variables needed to calculate the CRF components. The upwelling portion of the longwave and shortwave spectrum is ignored in the calculation of CRF. $L\uparrow$ is assumed to be the same with and without a cloud, as in Shupe & Intrieri (2004). $S\uparrow$ is ignored because the upwelling shortwave radiation is greatly influenced by changes in sea ice (i.e. albedo) and largely alters the values of CRF in the Arctic environment if included, as shown by Vavrus (2006). This definition of CRF only examines the instantaneous cloud effect. However, the cloud effect is not completely isolated from the surface in the Arctic (Dong et al. 2010, Stramler et al. 2011). For example, greater $L\downarrow$ will correspond with greater $L\uparrow$ values, because clouds act to warm the surface. Also, multiple reflections in the Arctic are common because of the persistent occurrence of clouds and a high surface albedo, which increase the $S\downarrow$ values.

We also analyzed basic thermodynamic and dynamic properties. Lower tropospheric stability affects boundary layer clouds (Klein & Hartmann 1993). In the Arctic, increased cloud cover occurs during periods with lower values of lower tropospheric stability (Kay & Gettelman 2009). We define the lower tropospheric stability (LTS) by Eq. (9)

$$\mathrm{LTS} = \Theta_{700} - \Theta_{\mathrm{surface}} \tag{9}$$

where Θ_{700} is the potential temperature at 700 hPa and $\Theta_{\mathrm{surface}}$ is the potential temperature at the surface. We also define low-level tropospheric stability (LLTS) following Kay & Gettleman (2009) as

$$\mathrm{LLTS} = \Theta_{925} - \Theta_{\mathrm{surface}} \tag{10}$$

where Θ_{925} is the potential temperature at 925 hPa. In addition, we analyzed lower tropospheric moisture advection (LTMA) by Eq. (11)

$$\mathrm{LTMA} = \frac{\int_{\mathrm{surface}}^{700} V_h \cdot \nabla Q \, \mathrm{d}P}{\int_{\mathrm{surface}}^{700} \mathrm{d}P} \tag{11}$$

and low-level tropospheric moisture advection (LLMA) by Eq. (12)

$$\mathrm{LLMA} = \frac{\int_{\mathrm{surface}}^{925} V_h \cdot \nabla Q \, \mathrm{d}P}{\int_{\mathrm{surface}}^{925} \mathrm{d}P} \tag{12}$$

In Eqs. (11 & 12), V_h is the horizontal wind velocity, Q is specific humidity and P is pressure.

Most radiative and cloud variables are reported as monthly averages using all periods of sky conditions (cloudy and clear). Exceptions include cloud base and cloud thickness. The monthly averages of these variables only represent periods when a cloud is present. Because Polar WRF archives data every 2 h, we define a cloud frequency variable as the amount of time the cloud is present anywhere in an atmospheric column divided by the total time, using the 2 h WRF output.

4. RESULTS

4.1. Near-surface temperature, radiation, and energetic fluxes

Increased near-surface temperatures occur during low sea ice cover years in the Laptev Sea (Fig. 3). The spatial variability of these differences (Fig. 3)

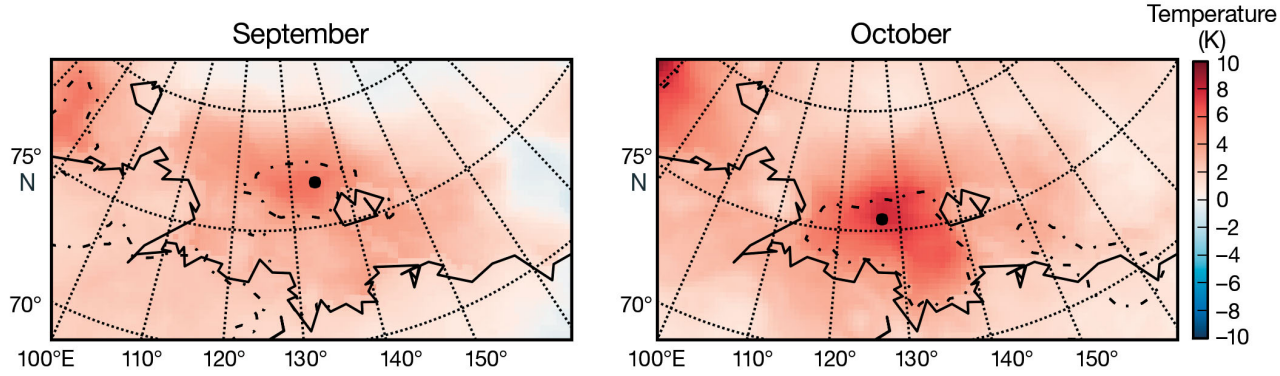

Fig. 3. Monthly averaged Polar WRF 2 m temperature (K) during low minus high sea ice cover years. The dot-dash line contours regions with $p < 0.05$. The dots represent the area with the greatest sea ice difference between the low and high years. These locations are at 77.36° N, 134.47° E for September and 75.97° N, 127.10° E for October

Table 2. Differences between flux terms during the averaged low and high sea ice cover years. All units are in W m^{-2}, and negative numbers represent less energy at the surface during low sea ice years. The variables are averaged around a 100 × 100 km region near 77.36° N, 134.47° E in September and 75.97° N, 127.10° E in October. See Section 3 for abbreviations

	Q	Q_{rad}	L_{net}	$L\downarrow$	$L\uparrow$	S_{net}	$S\downarrow$	$S\uparrow$	LH	SH	CRF_{total}	CRF_{LW}	CRF_{SW}
September	−21	7	−9	16	−26	16	−14	30	−12	−15	−7	4	−12
October	−80	−6	−7	31	−40	2	−3	4	−26	−48	21	23	−2

is very similar to that of ice cover (Fig. 2). When comparing the low and high sea ice ensembles, the difference in 2 m air temperature is greater in October than in September. As shown in Fig. 3, the maximum sea ice difference in September is centered at 77.36° N, 134.47° E, and the maximum difference in October is centered at 75.97° N, 127.10° E. Monthly mean values are given for these locations (Table 2).

Changes in the surface temperature may result from and cause differences in the surface radiative and energy budgets (Miller & Russell 2002, Schweiger et al. 2008a). Downwelling longwave radiation is greater during low sea ice years. The maximum longwave difference occurs at the site of maximum sea ice cover difference (Fig. 4). As with the changes in 2 m atmospheric temperature, greater differences occur in October than September. The $L\downarrow$ difference

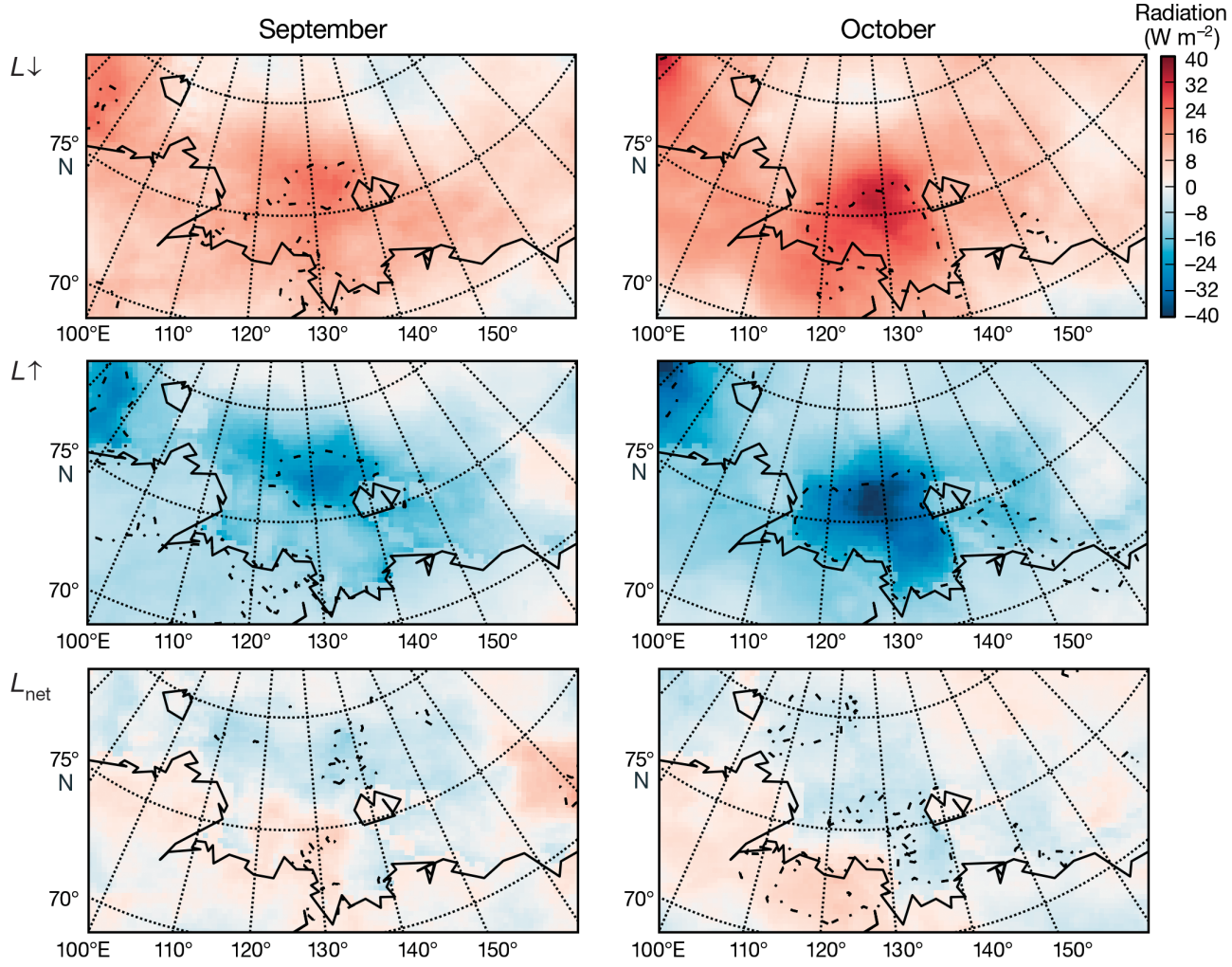

Fig. 4. As Fig. 3, but for the monthly averaged Polar WRF longwave radiative budget (W m^{-2}) at the surface. Changes in (top) downwelling flux $L\downarrow$, (middle) upwelling flux $L\uparrow$, and (bottom) net surface flux L_{net}; red areas indicate more energy toward the surface during low sea ice years. Differences are multiplied by the positive or negative sign in Eq. (4)

at the location of maximum change in sea ice in September is 16 W m^{-2}, while the October difference is 31 W m^{-2}. The upward longwave radiative fluxes at the surface are greater during years with low sea ice. In September, the difference is 26 W m^{-2}, and in October, the difference is 40 W m^{-2}. Differences in the net longwave flux (i.e. $L\downarrow - L\uparrow$) between low and high sea ice years are small in September and October.

Changes in the downwelling shortwave radiative fluxes are not as large between low and high sea ice years as changes in the longwave fluxes (Fig. 5). In addition, insolation greatly decreases in October compared to September, such that October differences in the shortwave are minimal. In September, increased values of both surface $S\downarrow$ and $S\uparrow$ occur during the high sea ice years. This corresponds with more solar radiation reaching the surface and being reflected from the surface during years with high sea ice. In September during low sea ice years, shortwave radiation reaching the surface ($S\downarrow$) is decreased by 14 W m^{-2} relative to high sea ice years. In October, this difference is near 3 W m^{-2}. The net shortwave budget (i.e. $S\downarrow - S\uparrow$) is positive in September. About 16 W m^{-2} is added to the surface during low sea ice years. However, the magnitude of this flux is dependent on the albedo of sea ice. A change in solar zenith angle (and hence location) will alter these results.

As anticipated, more latent and sensible heat leaves the surface in September and October during years with low sea ice than during years with high sea ice (Fig. 6). As with the near-surface temperature and longwave fluxes, these differences are greater in October than in September. Sensible heat flux changes are larger than the latent heat flux differences, with a

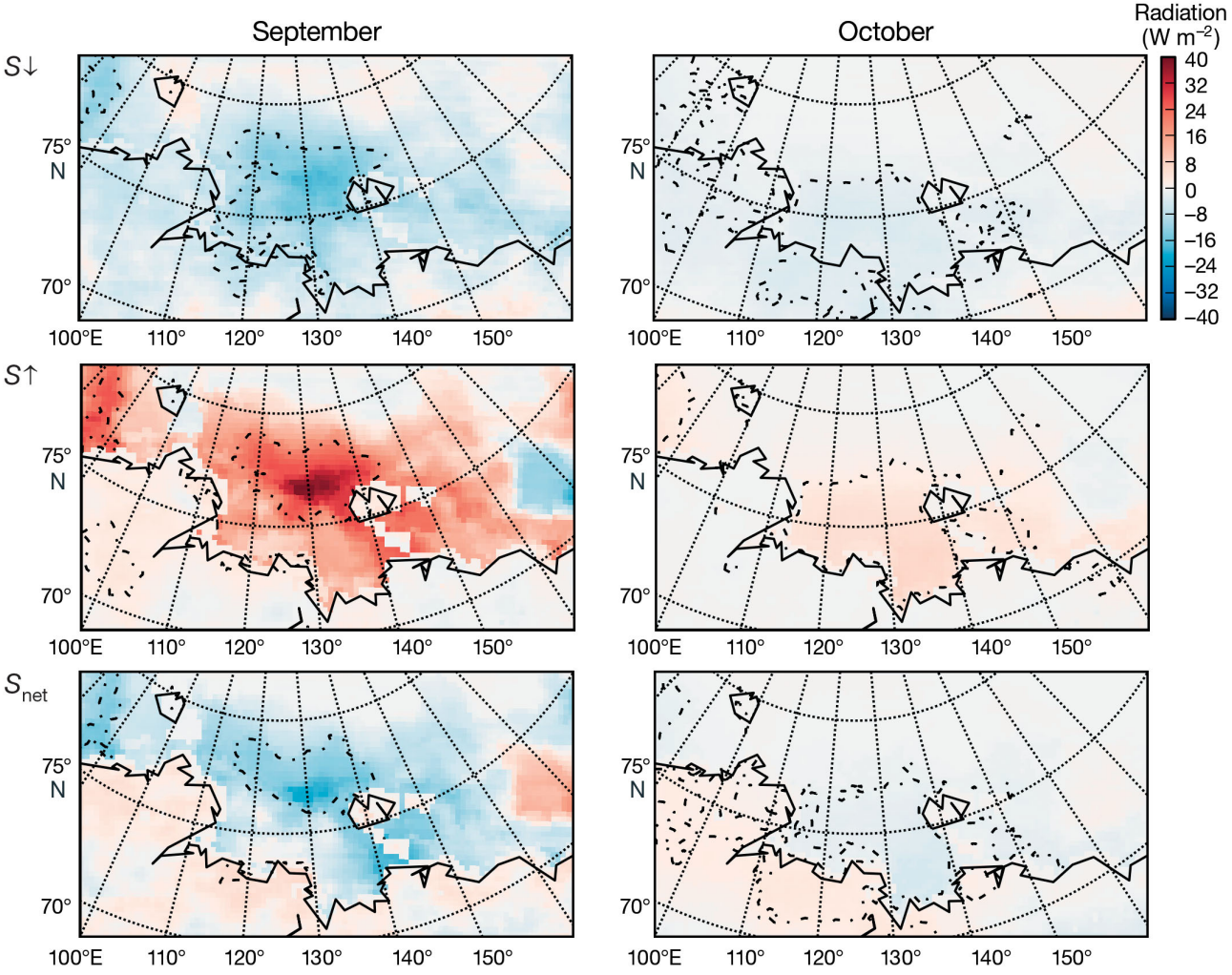

Fig. 5. As Fig. 3 for monthly averaged Polar WRF shortwave radiative budget (W m^{-2}) at the surface. Changes in (top) $S\downarrow$, (middle) $S\uparrow$, and (bottom) S_{net}; all red areas indicate more energy toward the surface during low sea ice years. Differences are multiplied by the positive or negative sign in Eq. (4)

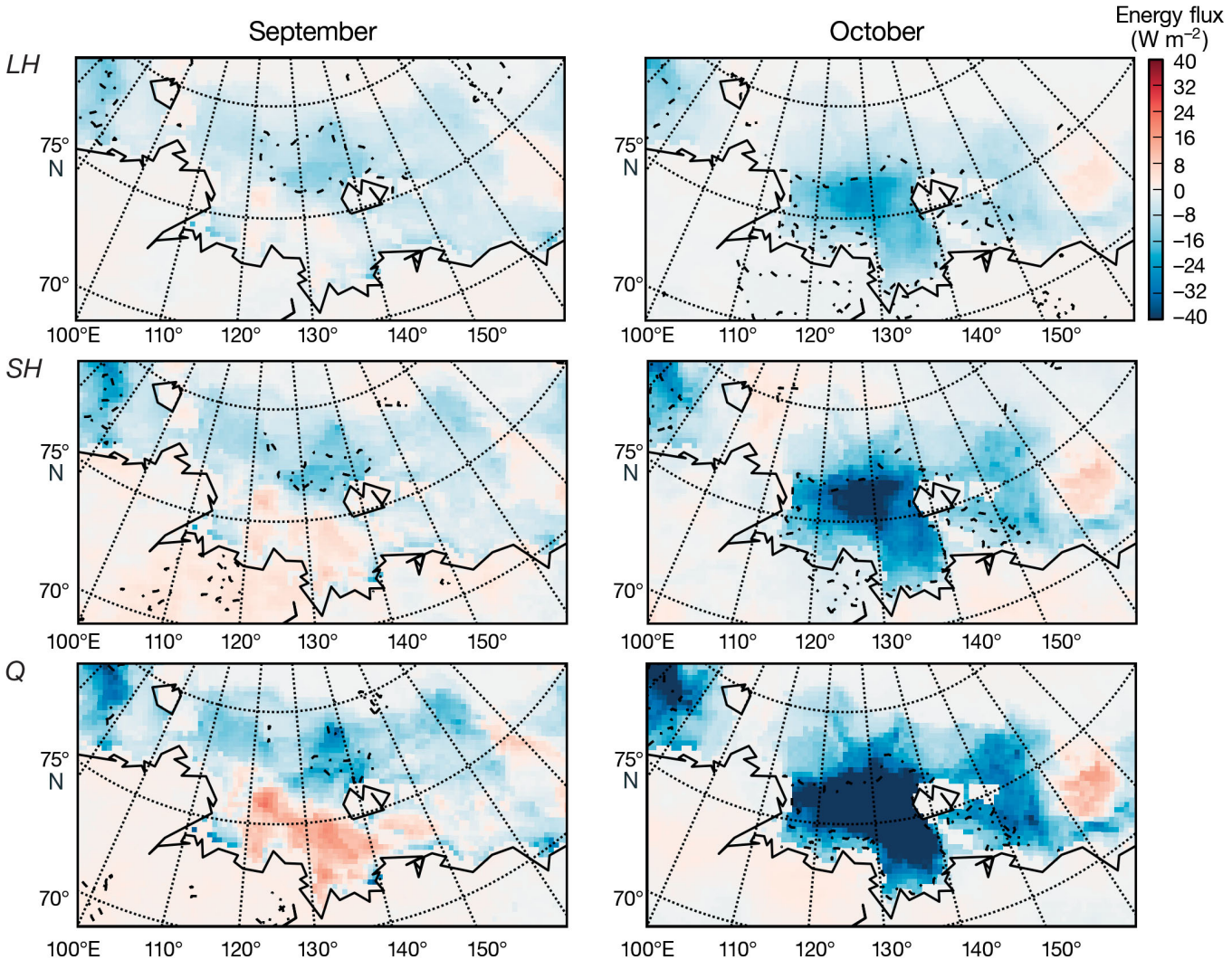

Fig. 6. As Fig. 3 for monthly averaged Polar WRF (top) latent heat flux (*LH*), (middle) sensible heat flux (*SH*), and (bottom) net surface energy flux (*Q*) (W m^{-2}) at the surface. Changes in (top) *LH*, (middle) *SH*, and (bottom) *Q*; red areas indicate more energy toward the surface during low sea ice years, i.e. the differences are multiplied by the positive or negative sign in Eq. (5)

difference in September of 15 W m^{-2} and in October of 48 W m^{-2}. More heat in terms of turbulent fluxes leaves the surface during low sea ice years.

The increased turbulent heat flux leaving the surface in October during low sea ice years affects the net energy flux (*Q*, Eq. 5). The decreased net energy fluxes during September for low sea ice years minus high sea ice years are near 21 W m^{-2}, while the difference in October is near 80 W m^{-2} at the locations of maximum sea ice difference. This increased energy leaving the surface during low sea ice years is almost entirely due to the turbulent heat flux. The changes in Q_{rad} (Fig. 7) in the low minus high sea ice composites are small. In October, the change is ~6 W m^{-2}, with less surface energy toward the surface during low sea ice years. In September, the change is 7 W m^{-2}, with more net surface energy during low sea ice years in Polar WRF. The September differences are statistically significant, while the October differences are not. The differences in the flux values are summarized in Table 2.

In September, there are positive net energy (*Q*) differences between low and high sea ice years near the Russian coast. This region has smaller sea ice cover differences (e.g. Fig. 2) than locations just to the north. Positive *Q* values are also shown in September and October east of 160° E, where differences in sea ice cover during the chosen years were relatively small. These changes are not significant at the 0.05 confidence level.

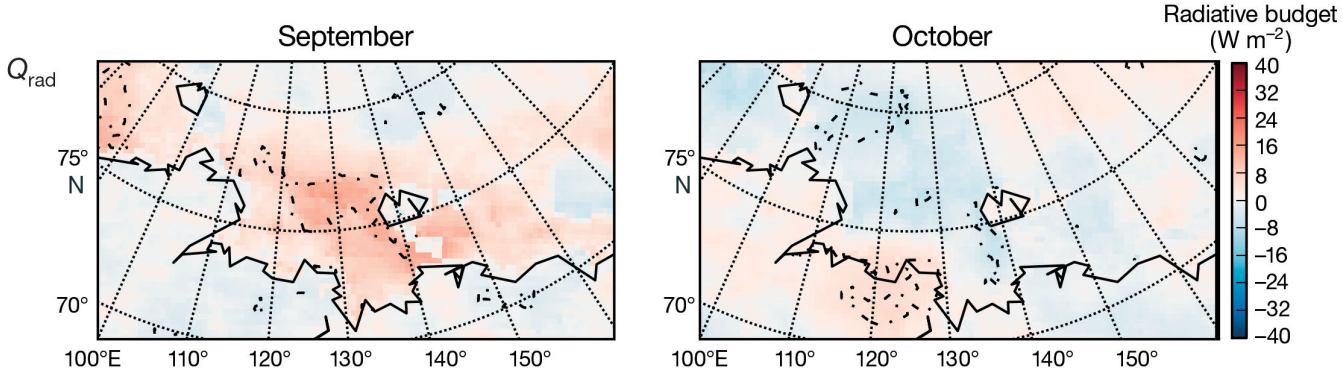

Fig. 7. As Fig. 3 for monthly averaged differences in Polar WRF net radiative budget, (W m^{-2}) at the surface; red areas indicate more energy toward the surface during low sea ice years. Differences are multiplied by the positive or negative sign in Eq. (4)

4.2. Cloud properties

Many of the above radiative changes can be explained by differences in temperature or albedo. For example, during the low sea ice years, higher surface temperatures occur and cause greater upwelling longwave radiative flux. However, the changes in downwelling longwave and shortwave radiation cannot be fully explained by temperature or albedo; some of these differences may instead be caused by changes in cloud occurrence or cloud properties.

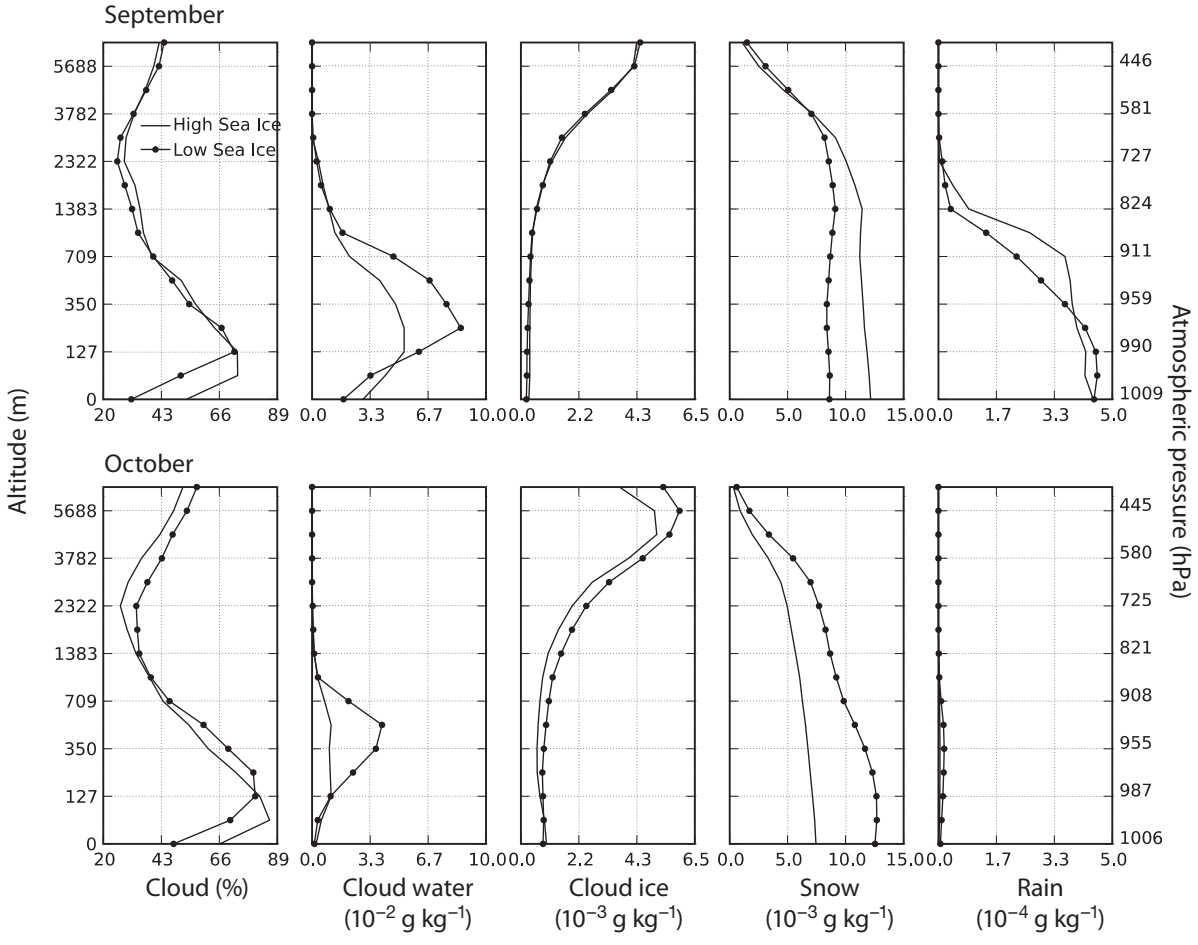

Fig. 8. Monthly averaged profiles of cloud fraction (%), cloud water mixing ratio (g kg^{-1}), cloud ice mixing ratio (g kg^{-1}), snow mixing ratio (g kg^{-1}), and rain mixing ratio (g kg^{-1}) for low and high sea ice years

Table 3. Cloud properties during low and high sea ice years. Variables are liquid water path (LWP), cloud frequency, cloud base, cloud thickness, and cloud base temperature. The variables are averaged around a 100 × 100 km region near 77.36° N, 134.47° E in September and 75.97° N, 127.10° E in October

		LWP ($g\ m^{-2}$)	Frequency (%)	Base (m)	Thickness (m)	Base temp. (K)
September	Low	64	77	422	535	269
	High	44	70	240	498	265
October	Low	23	52	187	429	257
	High	9	29	216	336	251

In September and October during years of high sea ice, Polar WRF produces increased cloud cover (%) in the lowest vertical levels (Fig. 8). Increased cloud fraction during high sea ice years occurs below ~130 m or ~990 hPa. Above this level, cloud cover percentages are fairly similar in September, with slightly greater cloud cover during the high sea ice years. However, in October, cloud cover above 127 m (990 hPa) is greater in the low sea ice years.

During low sea ice Septembers, the cloud water mixing ratio decreases notably below 100 m (980 hPa) (Fig. 8). In October, the cloud water mixing ratios below 127 m (987 hPa) are similar for both the low and high sea ice years. However, above 127 m (987 hPa) to ~1 km (850 hPa), the cloud water mixing ratios greatly increase during low sea ice years in both months. This increase in cloud mixing ratio is also shown in increases in LWP during low sea ice years (Table 3). The relative increase in LWP in October is much greater than the relative increase in September.

Cloud frequency is similar in low and high sea ice years for September, but larger differences occur in October (Table 3). This result is consistent with the LWP changes and the radiative surface flux changes. The cloud base is higher during low sea ice Septembers but lower during low sea ice Octobers. At first, this result seems inconsistent with the changes in cloud fraction and boundary layer changes (Table 4), but the cloud thickness increases during the low sea ice years in September and October (Table 3), with a larger percent increase in October. Because of the interplay between the cloud base and ambient temperature, there are not large differences between the cloud base temperature in September or October (Table 3).

The changes in average cloud ice amount between low and high sea ice years are close to zero for September (Fig. 8). In October, the ice mixing ratio is slightly larger during low sea ice years. The difference in October generally occurs at heights above 700 m. The snow mixing ratio in September is greater during high sea ice years. This is due to the atmospheric column being colder during these periods (Fig. 9). In October, the snow mixing ratio is greater during low sea ice years. This result is due to atmospheric column being cold enough to snow and more moisture being available than during high sea ice years. The rain mixing ratio is slightly larger during low sea ice years at the lowest atmospheric levels in September, due to the warmer lower atmosphere during those years (Fig. 9).

4.3. Dynamic and thermodynamic properties

Dynamic and thermodynamic variables are altered during low and high sea ice years. The changes in the vertical profile of cloud fraction and cloud mixing ratio are consistent with changes in the boundary layer height (Table 4). The thickness of the boundary layer increases during low sea ice years in both September and October, but the percentage increase is much greater in October. In September, the upward shift in the boundary layer height corresponds with an upward shift in the cloud base height. In October, the cloud base height does not rise when sea ice is removed.

The boundary layer is much more sensitive to changes in sea ice cover in October than in September, and this is indicated by larger differences in

Table 4. Averaged atmospheric properties during low and high ice years. From left to right, the variables (and units) are planetary boundary layer (PBL) height (m), lower tropospheric stability (LTS) defined at 700 hPa (K), low-level tropospheric stability (LLTS) defined at 925 hPa (K), mass weighted lower tropospheric moisture advection (LTMA) from the surface to 700 hPa ($g\ kg^{-1}\ d^{-1}$), and mass weighted low-level moisture advection (LLMA) from the surface to 925 hPa ($g\ kg^{-1}\ d^{-1}$). The variables are averaged around a 100 × 100 km region near 77.36° N, 134.47° E in September and 75.97° N, 127.10° E in October

		PBL height (m)	LTS (K)	LLTS (K)	LTMA ($g\ kg^{-1}\ d^{-1}$)	LLMA ($g\ kg^{-1}\ d^{-1}$)
September	Low	552	19	5	−0.31	−0.24
	High	445	23	9	0.089	0.18
October	Low	643	20	8	−0.11	−0.07
	High	287	27	14	−0.10	−0.10

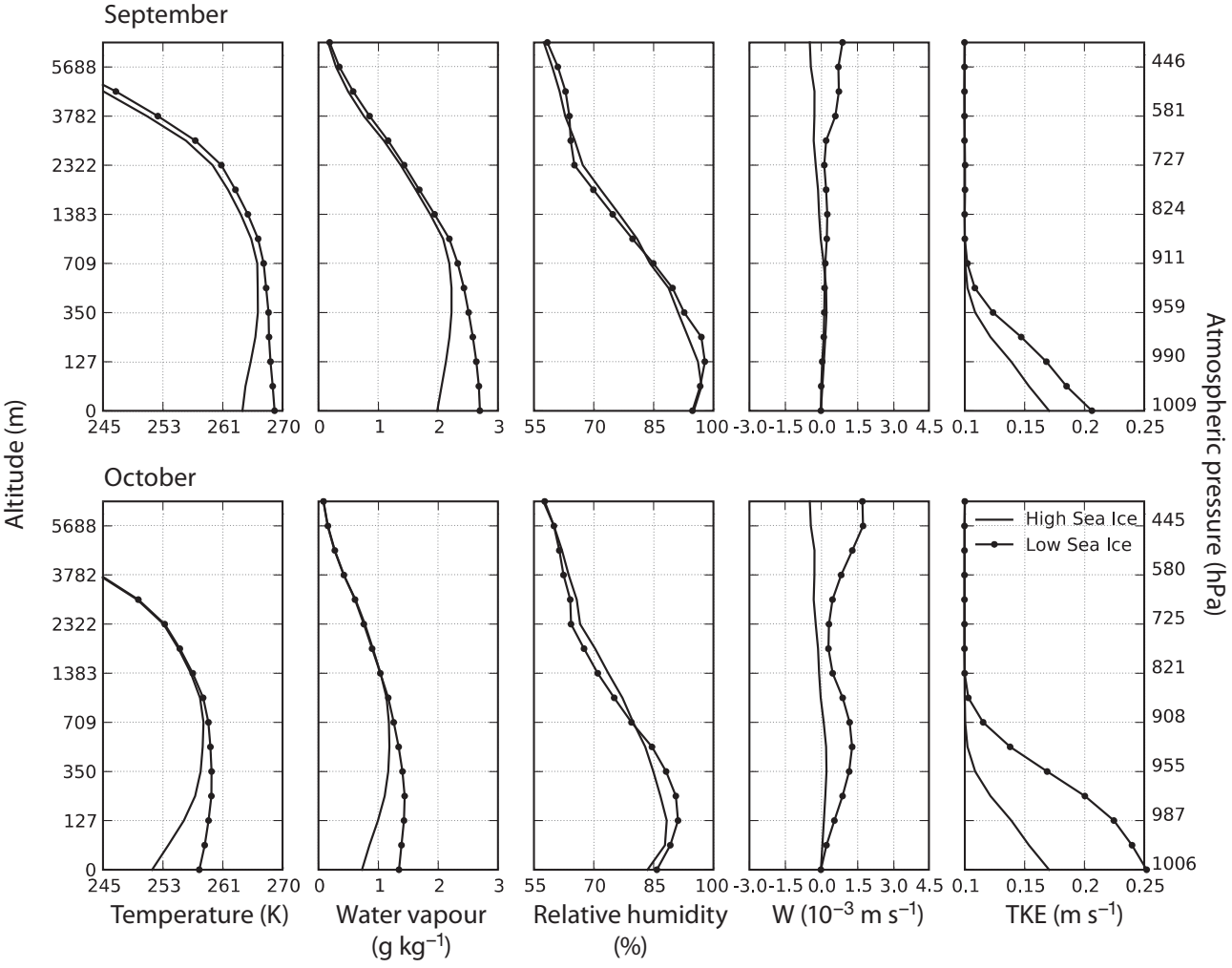

Fig. 9. Monthly averaged profiles of temperature (K), water vapor (g kg^{-1}), relative humidity (%), uplift (W; m s^{-1}), and turbulent kinetic energy (TKE; m^2 s^{-2}) for low and high sea ice years

the turbulent kinetic energy during October relative to September between low and high sea ice years (Fig. 9). Increased cloud cover frequently occurs during periods of lower tropospheric stability in the Arctic (Table 4). The percent increase in lower tropospheric stability in October is not much greater than the percent increase in September.

Other variables may contribute to the increased cloud LWP. As shown in Table 4, there is not much change in the low-level moisture advection. In September, there is more moisture advection in the high sea ice years, and insignificant changes occur in October. This result may be caused by the local increase in moisture during low sea ice years. In September and October during low sea ice years, there is an increase in relative humidity in the atmospheric levels below ~700 m (911 hPa) (Fig. 9). The relative increase is greater in October than in September and may help to explain the relative differences in cloud LWP. In addition, greater uplift occurs within the boundary layer during October low sea ice composites (Fig. 9). This uplift weakens just above the boundary layer in October. In September, there are not many differences in the uplift between the low and high sea ice composites. In the high sea ice Septembers and Octobers, atmospheric levels above ~1400 m (825 hPa) exhibit downward motion. This greater mid-level subsidence during high sea ice years is consistent with Cuzzone & Vavrus (2011).

During low sea ice years, there are insignificant increases in the temperature throughout the atmosphere in September, while the increase in temperature is limited to the boundary layer in October (e.g. Fig. 9). This corresponds to increases in water vapor throughout the atmospheric column during low sea ice Septembers and increases in Q_{rad} (e.g. Fig. 7).

4.4. Cloud radiative effect

In October, low sea ice years have more CRF_{LW} than high sea ice years (Fig. 10), with a difference of 23 W m^{-2} at the location of maximum sea ice difference. This difference in CRF_{LW} between September and October is most likely due to the saturation effect that LWP has on the longwave cloud radiative forcing (Shupe & Intrieri 2004, Chen et al. 2006). Once clouds have liquid water paths > ~30 g m^{-2}, the cloud acts as a blackbody (Shupe & Intrieri 2004), and additional changes in liquid amount do not affect the longwave radiation. In October, high sea ice years have LWPs ~9 g m^{-2} while during low sea ice years, the LWPs are near 23 g m^{-2}. Therefore, the change in LWP affects the emitted longwave radiation of a cloud to a much greater extent in October than in September. In addition, the cloud frequency (Table 3) does not change much within the September composite, while the cloud frequency changes to a greater extent in October. Relative changes in cloud base temperature between low and high sea ice Septembers and Octobers do not greatly differ. Thus, changes in LWP and cloud frequency may be more important than cloud temperature for changing the radiative budget in this experiment.

In October, the CRF_{SW} differences between high and low sea ice years are small (~2 W m^{-2}) (Table 2), due to the waning shortwave input from the sun. In October, low sea ice years have greater CRF_{total} by ~21 W m^{-2} than the high sea ice years, and these differences in the cloud radiative forcing are due to the longwave effect of the clouds. Because the shortwave effect of clouds greatly depends on the solar zenith angle, these results will not be representative of other latitudes and times.

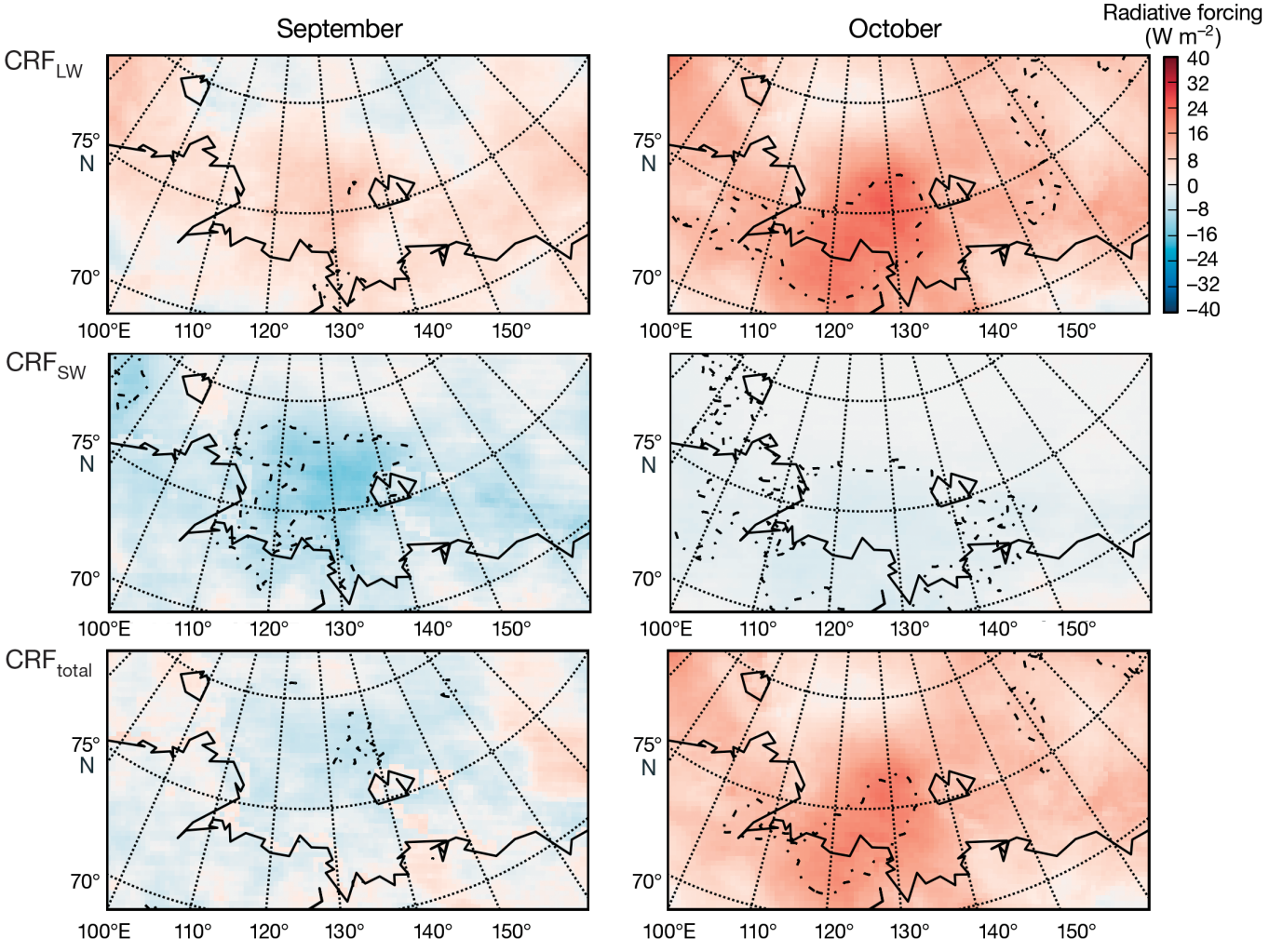

Fig. 10. Same as Fig. 3 for monthly averaged Polar WRF cloud radiative forcing (CRF) at the surface (W m^{-2}). Changes in (top) longwave (CRF_{LW}), (middle) shortwave (CRF_{SW}), and (bottom) total CRF (CRF_{total}); red areas indicate more energy toward the surface during low sea ice years

There are significant differences in CRF_{SW} (~12 W m^{-2}) between high and low sea ice Septembers (Fig. 10, Table 2). The decrease in CRF_{SW} during low sea ice years is a result of a higher cloud frequency and slightly higher LWPs. September differences in CRF_{LW} are small, with slightly greater values in the low sea ice years. Though low sea ice years in September do not display much more surface CRF_{LW} than the high sea ice years, low sea ice Septembers do have statistically significant greater amounts of $L\downarrow$. This suggests that there are other components besides clouds that affect the downwelling longwave fluxes. The clear sky water vapor values are greater during low sea ice years. In September, the shortwave and longwave cloud radiative effects have opposing signs so that CRF_{total} is nearly zero.

4.5. Role of sea ice at submonthly scales

To study submonthly differences, a 100 × 100 km region is examined. Four adjacent Polar WRF grid points are averaged and centered at 75.28° N, 127.86° E, the region of greatest differences in October sea ice cover. Polar WRF outputs data every 2 h, and a 3 d running average is calculated and displayed to reduce noise.

When sea ice begins to form in the low sea ice years, $L\downarrow$ and CRF_{LW} decrease simultaneously or within 2 d in Polar WRF (Fig. 11). The variability between the $L\downarrow$ and 2 m air temperature is related to changes in sea ice cover. Surface temperature values are generally >265 K when there is open ocean. These relationships are more easily observed in the low sea ice years, but they also occur during the high sea ice years. The lower troposphere becomes more stable when the sea ice increases and the 2 m air temperature decreases. Similar results have been shown by Pavelsky et al. (2011).

The variability of cloud LWP at submonthly time scales is much greater in magnitude than changes in $L\downarrow$. The monthly averaged LWP differences in October are due to the few days with zero or near zero sea ice. Once sea ice cover are near 90% in the high and low sea ice years, LWP values are generally <15 g m^{-2} and always <30 g m^{-2}. CRF_{SW} values increase (or are less effective at cooling the surface) until the insolation wanes, and there does not seem to be much variability in CRF_{SW} directly connected with the amount of open water.

Changes in the turbulent heat fluxes are very closely timed with changes in the PBL height; the lowest values of latent heat fluxes correspond with the highest PBL heights (Fig. 11). This relationship also occurs with the sensible heat flux (data not shown). When there is open water, SH and LH fluxes decrease (i.e. increasingly leave the surface) throughout the autumn until sea ice begins to form. Once sea ice forms, SH and LH fluxes become near zero, and the PBL height is sharply reduced. The changes in the PBL height are not related to changes in lower tropospheric stability. Though shortwave radiation reaching the surface is not zero at this point, it decreases slightly near the time that the PBL height sharply increases.

A strong connection between cloud water amount and boundary layer height is implied in monthly or seasonally averaged data, but the temporal variability is less connected in submonthly data. Increases in cloud LWP and $L\downarrow$ do not occur when the fluxes of SH and LH alter at the end of September and beginning of October. During the low sea ice years, the variation in $L\downarrow$, 2 m air temperature, and lower tropospheric stability is more consistently timed with changes in sea ice cover than with changes in the upward heat flux.

5. DISCUSSION

Polar WRF produces similar variability in temperature and radiative fields between low and high sea ice years as other modeling and observational studies (Manabe & Bryan 1985, Schweiger et al. 2008a, Deser et al. 2010, Strey et al. 2010). The removal of sea ice in Polar WRF leads to a warming of the lower atmosphere and a large release of latent and sensible heat from the surface. Increases in upwelling longwave radiation associated with less sea ice and higher surface temperatures balance the increases in downwelling longwave radiation caused by increased clouds and low-level moisture.

Several studies examined the local cloud response to changes in sea ice cover (Schweiger et al. 2008a, Kay & Gettelman 2009, Palm et al. 2010, Cuzzone & Vavrus 2011, Kay et al. 2011). Two of these studies used a climatological (>20 yr) compositing technique to examine the cloud response in the autumn, using reanalysis data (Schweiger et al. 2008a, Cuzzone & Vavrus 2011). One study examined 6 yr of active remotely sensed satellite data (Palm et al. 2010), and another study examined 3 yr of active and passive remotely sensed satellite data (Kay & Gettelman 2009). Kay et al. (2011) examined an idealized, data constrained, general circulation model simulation of the 2007 extreme sea ice extent event in July and

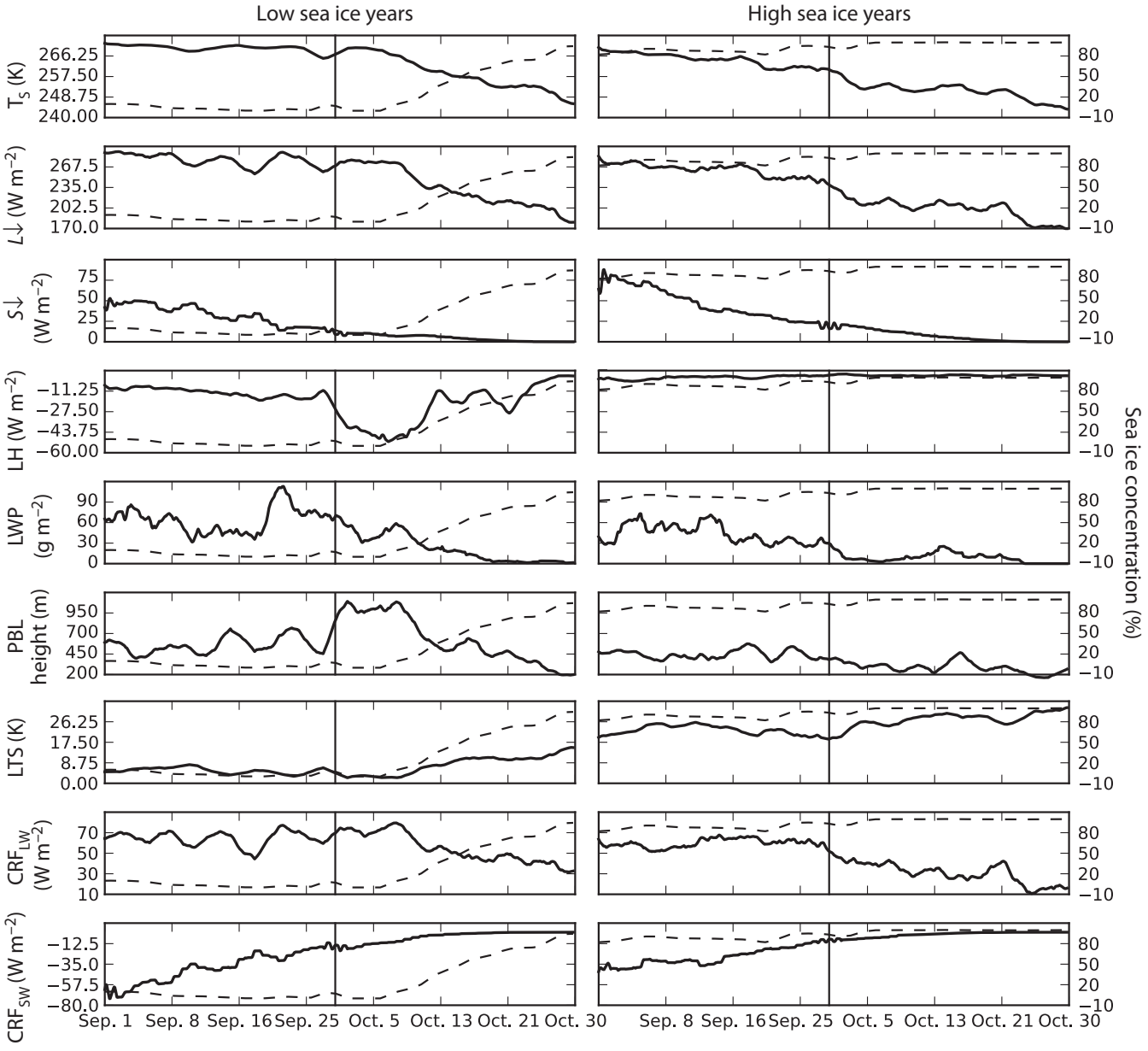

Fig. 11. From top to bottom, a 3 d running mean of 2 m temperature (T_S), surface $L\downarrow$, surface $S\downarrow$, latent heat flux (LH), cloud liquid water path (LWP), planetary boundary layer (PBL) height, lower tropospheric stability (LTS), surface CRF_{LW}, and surface CRF_{SW} for (left) low and (right) high sea ice years. Dashed line is the sea ice concentration. The left ordinate shows the variable unit, and the right ordinate shows sea ice concentration. The time series are averaged over a 100 × 100 km grid centered at 75.28° N, 127.86° E. All positive flux values represent energy toward the surface

September. Schweiger et al. (2008a) only reported low and middle cloud fractions. These cloud fractions are difficult to relate to the present study because our vertical resolution in WRF is much finer. Palm et al. (2010), Cuzzone & Vavrus (2011), and Kay et al. (2011) reported that the cloud amounts at the atmospheric levels closest to the surface are greater over sea ice than open water, due to a colder surface and the resulting higher relative humidity. Qualitatively, the results of the present study support Palm et al. (2010), Cuzzone & Vavrus (2011), and Kay et al. (2011). Kay & Gettelman (2009) found that the September and October averaged cloud amounts increase over open water at the lowest atmospheric levels. Qualitatively, our results are not similar to those of Kay & Gettelman (2009), but there are many differences among these studies including data sets, years of analysis, and compositing techniques.

More importantly, changes in cloud thickness and cloud liquid water paths influence changes in the surface radiative budget more than cloud fractions. Palm et al. (2010) reported increases in cloud optical thickness when the cloud is over open water compared to sea ice. Kay et al. (2011) also reported increases in cloud liquid water paths when a cloud forms over open water. Our results support Palm et al. (2010) and Kay et al. (2011). The relative change in the shortwave cloud effect between July and September found by Kay et al. (2011) is similar to the results of the present study. Insolation greatly affects the net change in the surface cloud radiative effect.

6. CONCLUSIONS

The relative change of 2 m air temperature, surface longwave radiation, turbulent heat fluxes, liquid water paths, and surface cloud radiative forcing between low and high sea ice composites is greater in October than in September. Only variables related to insolation have greater relative changes in September. This is shown in the positive surface radiative budget differences in September and not October. This increase in net surface radiation is caused by the reduced upward shortwave flux, i.e. albedo, in the high sea ice years. The insolation values and the resulting surface radiative fluxes are greatly dependent on location, and these results may not be representative across the Arctic domain. Low sea ice Septembers are associated with greater temperatures and more moisture throughout the atmospheric column than the high sea ice Septembers.

Changes in the cloud liquid water paths and cloud thickness are more important to the radiative budget than cloud fraction differences. In October, the relatively large amount of change is associated with clouds significantly warming the surface. In September, the cloud property changes are not large enough to significantly alter the longwave cloud effect on the surface; clouds slightly cool the surface during low sea ice years in the shortwave, but the total radiative effect of cloud changes between Septembers with high and low sea ice extent is near zero.

PBL height varies with latent and sensible heat fluxes at short time scales (days). This is more apparent during open water periods, and the connection between turbulent heat fluxes and PBL height is increasingly evident later in the autumn. Variability in lower tropospheric stability, surface temperature, surface longwave downward values, and the longwave cloud effect on surface temperature are tied to the sea ice cover.

Acknowledgements. N.P.B. contributed to this work under the auspices of the U.S. Department of Energy by Lawrence Livermore National Laboratory (LLNL) under contract DE-AC52-07NA27344. This work was funded, in part, by the University of Delaware's Office of Graduate and Professional Education fellowship and in part by the LLNL Institutional Postdoc Program. We thank the 3 anonymous reviewers for greatly aiding in the improvement of this paper.

LITERATURE CITED

Beesley JA (2000) Estimating the effect of clouds on the arctic surface energy budget. J Geophys Res D 105: 10103–10117

Bromwich DH, Hines KM, Bai LS (2009) Development and testing of Polar Weather Research and Forecasting model: 2. Arctic Ocean. J Geophys Res D 114:D08122

Chen F, Dudhia J (2001) Coupling an advanced land surface-hydrology model with the Penn State-NCAR MM5 modeling system. Part I: Model implementation and sensitivity. Mon Weather Rev 129:569–585

Chen YH, Aires F, Francis JA, Miller JR (2006) Observed relationships between arctic longwave cloud forcing and cloud parameters using a neural network. J Clim 19: 4087–4104

Collins WD, Rasch PJ, Boville BA, Hack JJ and others (2006) The formulation and atmospheric simulation of the Community Atmosphere Model version 3 (CAM3). J Clim 19: 2144–2161

Curry JA, Ebert EE (1992) Annual cycles of radiation fluxes over the Arctic Ocean: sensitivity to cloud optical properties. J Clim 5:1267–1280

Curry JA, Schramm JL, Ebert EE (1993) Impact of clouds on the surface radiation balance of the Arctic Ocean. Meteorol Atmos Phys 51:197–217

Cuzzone J, Vavrus S (2011) The relationships between Arctic sea ice and cloud-related variables in the ERA-Interim reanalysis and CCSM3. Environ Res Lett 6:014016

Deser C, Tomas R, Alexander M, Lawrence D (2010) The seasonal atmospheric response to projected Arctic sea ice loss in the late twenty-first century. J Clim 23:333–351

DeWeaver ET, Hunke EC, Holland MM (2008) On the reliability of simulated Arctic sea ice in global climate models. Geophys Res Lett 35:2

Dong X, Xi B, Crosby K, Long CN, Stone RS, Shupe MD (2010) A 10 year climatology of Arctic cloud fraction and radiative forcing at Barrow, Alaska. J Geophys Res D 115:D17212

Eastman R, Warren SG (2010) Interannual variations of Arctic cloud types in relation to sea ice. J Clim 23:4216–4232

Grell GA, Devenyi D (2002) A generalized approach to parameterizing convection combining ensemble and data assimilation techniques. Geophys Res Lett 29:4

Hines KM, Bromwich DH (2008) Development and testing of Polar Weather Research and Forecasting (WRF) Model. Part I: Greenland ice sheet meteorology. Mon Weather Rev 136:1971–1989

Hines KM, Bromwich DH, Bai LS, Barlage M, Slater AG (2011) Development and testing of Polar WRF. Part III: Arctic land. J Clim 24:26–48

Hong SY, Juang HMH, Zhao QY (1998) Implementation of prognostic cloud scheme for a regional spectral model. Mon Weather Rev 126:2621–2639

Janjic ZI (1994) The step-mountain Eta coordinate model:

further developments of the convection, viscous sublayer, and turbulence closer schemes. Mon Weather Rev 122:927–945

Janjic Z (2002) Nonsingular implementation of the Mellor-Yamada Level 2.5 scheme in the NCEP Meso model. National Centers for Environmental Prediction, Office Note No. 437

Kanamitsu M, Ebisuzaki W, Woollen J, Yang SK, Hnilo JJ, Fiorino M, Potter GL (2002) NCEP-DOE AMIP-II reanalysis (R-2). Bull Am Meteorol Soc 83:1631–1643

Kay JE, Gettelman A (2009) Cloud influence on and response to seasonal Arctic sea ice loss. J Geophys Res D 114:D18204

Kay JE, Raeder K, Gettelman A, Anderson J (2011) The boundary layer response to recent Arctic sea ice loss and implications for high-latitude climate feedbacks. J Clim 24:428–447

Klein SA, Hartmann DL (1993) The seasonal cycle of low stratiform clouds. J Clim 6:1587–1606

Klingaman NP, Butke J, Leathers DJ, Brinson KR, Nickl E (2008) Mesoscale simulations of the land surface effects of historical logging in a moist continental climate regime. J Appl Meteorol Climatol 47:2166–2182

Manabe S, Bryan K (1985) CO_2-induced change in a coupled ocean–atmosphere model and its paleoclimatic implications. J Geophys Res C 90:1689–1707

Miller JR, Russell GL (2002) Projected impact of climate change on the energy budget of the Arctic Ocean by a global climate model. J Clim 15:3028–3042

Miller JR, Chen YH, Russell GL, Francis JA (2007) Future regime shift in feedbacks during Arctic winter. Geophys Res Lett 34:4

Morrison H, Curry JA, Khvorostyanov VI (2005) A new double-moment microphysics parameterization for application in cloud and climate models. Part I: Description. J Atmos Sci 62:1665–1677

Palm SP, Strey ST, Spinhirne J, Markus T (2010) Influence of Arctic sea ice extent on polar cloud fraction and vertical structure and implications for regional climate. J Geophys Res D 115:D21209

Paluch IR, Lenschow DH, Wang Q (1997) Arctic boundary layer in the fall season over open and frozen sea. J Geophys Res D 102:25955–25971

Pavelsky TM, Boe J, Hall A, Fetzer EJ (2011) Atmospheric inversion strength over polar oceans in winter regulated by sea ice. Clim Dyn 36:945–955

Perovich DK, Grenfell TC, Light B, Hobbs PV (2002) Seasonal evolution of the albedo of multiyear Arctic sea ice. J Geophys Res C 107:8044

Previdi M, Veron DE (2005) North Atlantic Oscillation-related climate variability in a regional atmospheric model. J Geophys Res D 110:D16106

Previdi M, Veron DE (2007) North Atlantic cloud cover response to the North Atlantic oscillation and relationship to surface temperature changes. J Geophys Res D 112:D07104

Ramanathan V, Cess RD, Harrison EF, Minnis P, Barkstrom BR, Ahmad E, Hartmann D (1989) Cloud-radiative forcing and climate: results from the Earth Radiation Budget Experiment. Science 243:57–63

Schweiger AJ, Lindsay RW, Vavrus S, Francis JA (2008a) Relationships between Arctic sea ice and clouds during autumn. J Clim 21:4799–4810

Schweiger AJ, Zhang J, Lindsay RW, Steele M (2008b) Did unusually sunny skies help drive the record sea ice minimum of 2007? Geophys Res Lett 35:6

Serreze MC, Francis JA (2006) The arctic amplification debate. Clim Change 76:241–264

Shine KP, Crane RG (1984) The sensitivity of a one-dimensional thermodynamic sea ice model to changes in cloudiness. J Geophys Res C 89:10615–10622

Shupe MD, Intrieri JM (2004) Cloud radiative forcing of the Arctic surface: the influence of cloud properties, surface albedo, and solar zenith angle. J Clim 17:616–628

Stramler K, Del Genio AD, Rossow WB (2011) Synoptically driven Arctic winter states. J Clim 24:1747–1762

Strey ST, Chapman WL, Walsh JE (2010) The 2007 sea ice minimum: impacts on the Northern Hemisphere atmosphere in late autumn and early winter. J Geophys Res D 115:13

Vavrus S (2004) The impact of cloud feedbacks on Arctic climate under greenhouse forcing. J Clim 17:603–615

Vavrus S (2006) An alternative method to calculate cloud radiative forcing: implications for quantifying cloud feedbacks. Geophys Res Lett 33:L01805

Wang XJ, Key JR (2003) Recent trends in Arctic surface, cloud, and radiation properties from space. Science 299: 1725–1728

Wilson AB, Bromwich DH, Hines KM (2011) Evaluation of Polar WRF forecasts on the Arctic System Reanalysis domain: surface and upper air analysis. J Geophys Res D 116:18

Editorial responsibility: Oliver Frauenfeld, College Station, Texas, USA

Submitted: March 8, 2011; Accepted: March 7, 2012
Proofs received from author(s): August 7, 2012